Precision comparison of the quantum Hall effect in graphene and gallium arsenide

2012 Metrologia 49 294

(http://iopscience.iop.org/0026-1394/49/3/294)

Metrologia **49** (2012) 294–306 doi:10.1088/0026-1394/49/3/294

Precision comparison of the quantum Hall effect in graphene and gallium arsenide

T J B M Janssen[1], J M Williams[1], N E Fletcher[2], R Goebel[2], A Tzalenchuk[1], R Yakimova[3], S Lara-Avila[4], S Kubatkin[4] and V I Fal'ko[5]

[1] National Physical Laboratory, Hampton Road, Teddington TW11 0LW, UK
[2] Bureau International des Poids et Mesures, Pavillon de Breteuil, F-92312, France
[3] Department of Physics, Chemistry and Biology (IFM), Linköping University, S-581 83 Linköping, Sweden
[4] Department of Microtechnology and Nanoscience, Chalmers University of Technology, S-412 96 Götenborg, Sweden
[5] Physics Department, Lancaster University, Lancaster LA1 4YB, UK

E-mail: jt.janssen@npl.co.uk

Received 4 November 2011, in final form 8 February 2012
Published 29 March 2012
Online at stacks.iop.org/Met/49/294

Abstract
The half-integer quantum Hall effect in epitaxial graphene is compared with high precision to the well-known integer effect in a GaAs/AlGaAs heterostructure. We find no difference between the quantized resistance values within the relative standard uncertainty of our measurement of 8.7×10^{-11}. The result places new tighter limits on any possible correction terms to the simple relation $R_K = h/e^2$, and also demonstrates that epitaxial graphene samples are suitable for application as electrical resistance standards of the highest metrological quality. We discuss the characterization of the graphene sample used in this experiment and present the details of the cryogenic current comparator bridge and associated uncertainty budget.

(Some figures may appear in colour only in the online journal)

1. Introduction

The discovery seven years ago of the quantum Hall effect (QHE) in graphene sparked an immediate interest in the metrological community [1, 2]. The QHE is a fascinating macroscopic quantum effect occurring in two-dimensional conductors and relates the resistance quantum, h/e^2, only to the fundamental constants of nature, h, the Planck constant, and e, the elementary charge [3]. Although the QHE has been used successfully in metrology to realize the resistance scale for more than two decades [4], graphene is a material with properties like no other. Graphene, a single layer of carbon atoms in a hexagonal crystal lattice structure, is a truly two-dimensional metal with a linear dispersion relationship characteristic of massless Dirac-type charge carriers [5]. The unique bandstructure of this semi-metal has both practical and fundamental implications. Firstly, the massless nature of the charge carriers leads to a Landau level (LL) spectrum with an energy gap between the first two levels which is around 5 times larger than that in semiconductor materials for magnetic fields around 10 T. This implies that the QHE in graphene can be observed at much reduced magnetic fields and/or much higher temperatures [6]. Secondly, the marked difference in bandstructure and charge carrier characteristics between graphene and semiconductor systems allows for a demonstration of the universality of the QHE through a rigorous test of the material independence of the value of R_K, the von Klitzing constant.

Theory predicts no measurable corrections to the simple relation $R_K = h/e^2$. The quantum Hall resistance is considered to be a topological invariant [7], not altered by the electron–electron interaction, spin–orbit coupling or hyperfine interaction with nuclei. It has also been shown that the quantized Hall resistance is insensitive to much more subtle influences of the gravitational field [8]. Recently, a quantum electrodynamical approach to charge carriers in a magnetic field has predicted a tiny correction to the von Klitzing constant of the order of 10^{-20} for practical magnetic field values [9]. However, the size of this predicted correction is about 10 to 8 orders of magnitude smaller than the most accurate measurement techniques available and therefore untestable. Nevertheless, the fundamental nature of the Hall resistance

quantization makes experimental tests of its universality of the utmost importance, in particular, for improving our knowledge of two fundamental quantities of nature: the elementary charge and the Planck constant. The precision obtained through a universality test as presented here is much greater than is possible by a comparison of the best values of the constants h, e and R_K [10]. Analysis of the complete set of published results carried out by CODATA [10] showed no deviation from h/e^2 to within 2×10^{-8}, which calls for more accurate measurements. Universality of R_K will strongly support the pending redefinition of the SI units for mass and current in terms of h and e [11].

A direct comparison of the Hall resistance in two different substances does not prove the exactness of the relationship $R_K = h/e^2$; however, material independence is a significant factor in establishing the fundamental nature of R_K. This material independence turns out to be rather difficult to establish. Indeed the characteristics of QHE samples must satisfy very stringent requirements [12] and in 30 years only silicon MOSFETs (metal–oxide–semiconductor field-effect transistors) and III–V (GaAs/AlGaAs or InGaAs/InP) heterostructures have done so.

The first accurate measurements of the QHE in graphene were performed by Giesbers *et al* [13] on exfoliated samples. The precision obtained in these measurements was 15 ppm and limited by the high (≈kΩ) contact resistances together with a small (≈2.5 μA) maximum source–drain current which these samples could sustain before breakdown of the QHE occurred. A large measurement current determines the maximum signal-to-noise ratio and increasing this breakdown current is key to high-resolution measurements. One established method of increasing the breakdown current is to increase the sample width [4], which is not easy to achieve with the exfoliation technique.

In 2009 a number of groups around the world almost simultaneously succeeded in growing large-area wafers of epitaxial graphene by sublimation of SiC with a quality good enough to observe the quantized Hall resistance [14–18]. In an indirect comparison with a GaAs/AlGaAs device via an intermediate room-temperature standard resistor, we demonstrated universality of R_K with an uncertainty of 3 parts in 10^9 [16]. The measurement system [19] was identical to that used by Giesbers *et al* [13] and the key factors in the improvement were the very low contact resistances and large sample size which were achieved, resulting in an order of magnitude increase in the breakdown current. Subsequently we undertook a direct comparison between epitaxial graphene and two GaAs/AlGaAs devices using a modified measurement system demonstrating equivalence to an accuracy of 8.6 parts in 10^{11} [20]. Recently, much progress has been made on metrological quantum Hall measurements in exfoliated graphene devices with accuracies continuously increasing to around 5 parts in 10^7 [21, 22].

In this paper we present a detailed description of the graphene device characterization, measurement system, data analysis and resulting uncertainty budget which underpins the direct comparison result [20].

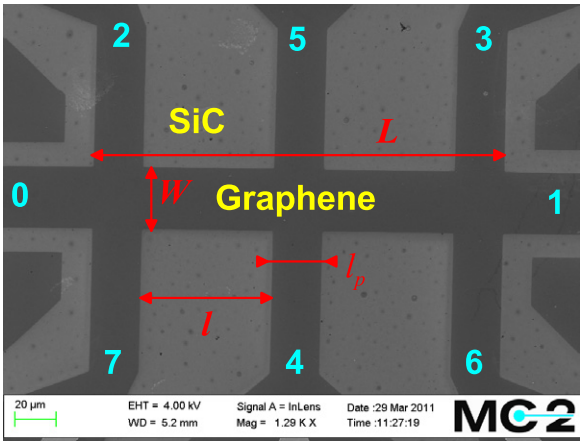

Figure 1. SEM image of a typical device and contact labels. The values for the parameters L, W, l and l_p are listed in table 2.

2. Characterization of epitaxial graphene

In [16] we reported the first accurate measurements of the quantum Hall effect in large high-quality epitaxial samples. The material studied in our experiments was grown on the Si-terminated face of a 4H-SiC(0 0 0 1) substrate [23]. The reaction kinetics on the Si-face are slower than on the C-face because of the higher surface energy, which helps homogeneous and well-controlled graphene formation. Graphene was grown at 2000 °C and 1 atm Ar gas pressure, which result in monolayers of graphene atomically uniform over more than 50 μm^2, as shown by low-energy electron microscopy. Twenty Hall bar devices of different sizes, from 160 μm × 35 μm down to 11.6 μm × 2 μm, were produced on each 0.5 cm^2 wafer using standard electron beam lithography and oxygen plasma etching (figure 1). Atomic force microscopy (AFM) images revealed that the graphene layer covers the substrate steps like a carpet, preserving its structural integrity [16]. Contacts to graphene were produced by straightforward deposition of 3 nm of Ti and 100 nm of Au through a lithographically defined mask followed by lift-off, with a typical area of graphene–metal interface of 10^4 μm^2 for each contact. Using transport measurements in low magnetic fields, we established that the manufactured material was n-doped, with the measured electron concentration in the range of 5.5×10^{11} cm^{-2} to 9×10^{11} cm^{-2}, mobility about 2400 cm^2 V^{-1} s^{-1} at room temperature and between 4000 cm^2 V^{-1} s^{-1} and 7500 cm^2 V^{-1} s^{-1} at 4.2 K, almost independent of device dimensions and orientation with respect to the substrate terraces. All results presented in this work were obtained on the largest Hall bar (i.e. 160 μm × 35 μm).

In fact epitaxial graphene grown on SiC is always strongly n-type doped with carrier densities typically in the range 10^{12} cm^{-2}–10^{13} cm^{-2}. The doping of the graphene is caused by the so-called 'dead layer' of carbon atoms in between the SiC substrate and graphene. This layer is non-conducting and characterized by a $6\sqrt{3} \times 6\sqrt{3}$ supercell of the reconstructed surface of sublimated SiC. Missing or substituted carbon atoms in various positions of such a huge supercell in the dead layer create localized surface states with a broad distribution of energies within the bandgap of SiC. It appears that the density

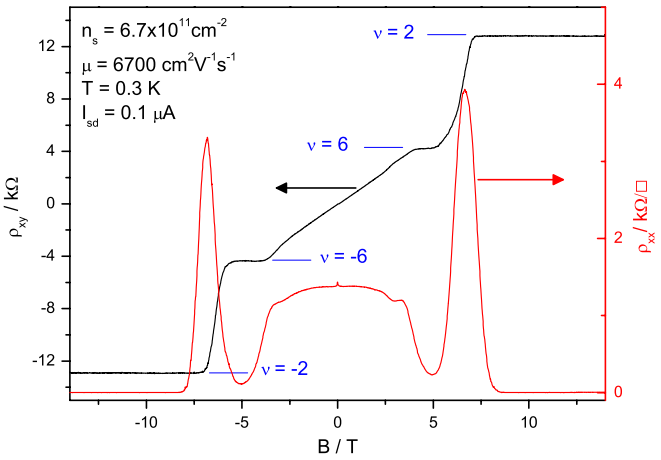

Figure 2. Transverse (ρ_{xy}) (contacts 4 and 5 in figure 1) and longitudinal (ρ_{xx}) (contacts 6 and 7) resistivity measurement. In all measurements in this work the source–drain current is between contacts 0 and 1. The horizontal lines indicate the exact quantum Hall resistivity values for filling factors $\nu = \pm 2$ and ± 6.

of such defects is higher in material grown at low temperatures (1200 °C to 1600 °C), resulting in graphene doped to a large electron density [24]. On the other hand, the material used in this work is grown at high temperatures in a highly pressurized atmosphere of Ar which seems to improve the integrity of the reconstructed 'dead' layer, leading to a lower density of donors on the surface and, therefore, producing graphene with a much lower initial doping [16, 25].

Figure 2 shows a typical measurement of the longitudinal and transverse resistivity as a function of magnetic flux density B at low temperatures. Wide plateaux are observed in the transverse resistivity which are accompanied by a vanishingly small value of the longitudinal resistivity. The sequence of quantum Hall plateaux and the absence of the $\nu = 4$ plateau confirm that the sample is monolayer graphene. At zero field a small weak localization peak is visible—a signature of quantum coherence in disordered Fermi liquid in epitaxial graphene [26]. Characteristic scattering lengths have been determined from the analysis of the weak localization correction to the Drude conductivity. For our graphene grown on SiC we find that the phase coherence length $L_\phi \approx 1\,\mu$m at low temperatures, the intervalley scattering length $L_i \approx 0.2\,\mu$m and the intravalley scattering length $L_* \approx 0.02\,\mu$m, the latter two being virtually temperature independent. These experimental scattering lengths set a limit of at least 50 ps on the spin relaxation time in this material.

For accurate quantum Hall measurements it is important that the contact resistance is well below ≈100 Ω [4]. Table 1 shows the measured contact resistances for our device and demonstrates that this condition is satisfied for most of the contacts. Our graphene device was approximately two years old at the time of these measurements and had been thermally cycled between 300 mK and room temperature more than a dozen times. Also the contacts have been re-bonded several times in the TO8-header which has caused damage to some of the bonding pads and is the most likely cause of the poor resistance of contacts 3 and 5 (on pristine devices we routinely get all contact resistances below 1 Ω).

Table 1. Three-terminal contact resistances measured at $B = 14$ T in the $\nu = 2$ quantum Hall state. The measurement current was 10 μA and a lead resistance of 2.7 Ω was subtracted.

Contact no	R/Ω
0	0.3
1	0.3
2	15
3	125
4	0.3
5	90
6	23
7	0.3

In order to extend the range of applicability the $\nu = 2$ quantum Hall plateau can be brought down in magnetic field by reducing the carrier density using a novel photochemical gating technique [25]. This is achieved by coating the device with a polymer bilayer, a spacer layer (PMMA) followed by an active polymer (ZEP520) able to generate potent electron acceptors under UV light exposure. The effect can be reversed by heating the sample to 170 °C just above the glass transition temperature of the polymer. Using this technique the carrier density of our device was reduced to 4.6×10^{11} cm^{-2}, resulting in an extremely wide $\nu = 2$ quantum Hall plateau as can be seen in figure 3(*b*).

Accurate quantum Hall resistance measurements require that the longitudinal voltage remains zero to ensure the device is in the non-dissipative state, which can be violated by the breakdown of the QHE at high source–drain current levels. Figure 3(*a*) shows the determination of the breakdown current I_c for different values of B along the $\nu = 2$ plateau. Here we define I_c as the source–drain current, I_{sd}, at which $V_{xx} \geqslant 100$ nV. Above the breakdown current the voltage increases rapidly as a function of current as a consequence of the sudden increase in electron temperature and subsequent increase in longitudinal resistivity [27]. In figure 3(*b*) the values of the breakdown current are plotted as a function of B together with ρ_{xx} and ρ_{xy}.

Figure 4 shows the measurement of V_{xx} as a function of I_{sd} at 11 T and 14 T in more detail (these are the magnetic flux densities at which the comparison measurements are performed). On the log–log plot it is clear that above the breakdown current the longitudinal voltage shows a power-law dependence on current. The red lines in the figure are a fit to this part of the trace. For the highest flux density of 14 T the breakdown current is ∼500 μA; however, the maximum source–drain current used in our comparison measurements is 100 μA. The extrapolated fitted line indicates that the expected V_{xx} is ∼1.3 pV at 100 μA and therefore $R_{xx} \approx 13$ nΩ. Note that close to the breakdown current V_{xx} drops away much more quickly than this power-law behaviour before it disappears in the noise of the DVM (±5 nV) (the shape of the breakdown curve is remarkably similar to that observed by Cage *et al* [28] for GaAs heterostructure devices) and therefore the $R_{xx} \approx 13$ nΩ is the upper bound. On the basis of this analysis we can be confident that the longitudinal resistivity is vanishingly small and that there is a considerable safety margin on I_{sd} in our experiments. A few measurements were performed at a lower

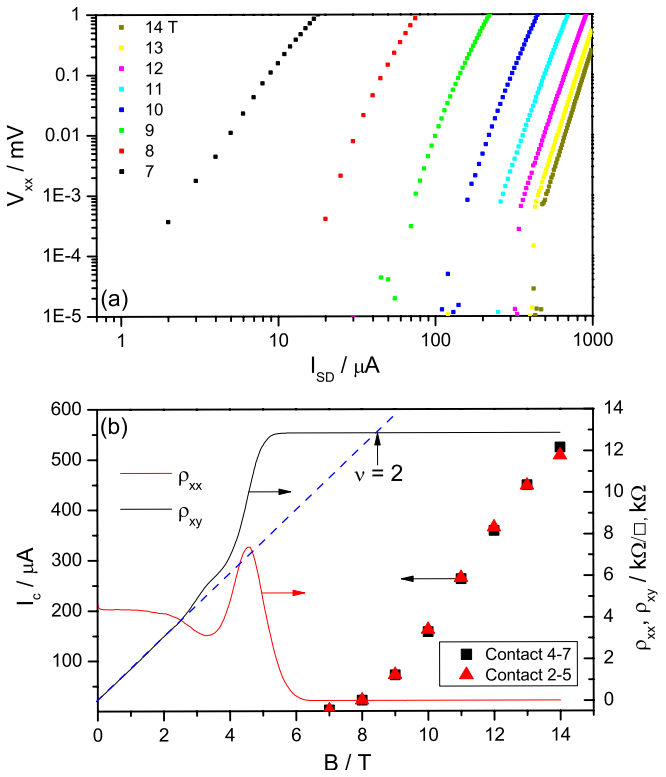

Figure 3. (a) Measurement of V_{xx} (contacts 4 and 7) as a function of source–drain current at different values of magnetic flux density ranging from $B = 7$ T (left hand curve) to 14 T (right curve) in steps of 1 T. (b) Transverse (ρ_{xy}) (contacts 4 and 5) and longitudinal (ρ_{xx}) (contacts 4 and 7) resistivity measurement at the reduced carrier density of 4.6×10^{11} cm^{-2} measured at $I_{sd} = 1\,\mu$A together with the measured breakdown current, I_c. Dashed blue line indicates position of the exact $\nu = 2$ filling factor for the low field carrier density.

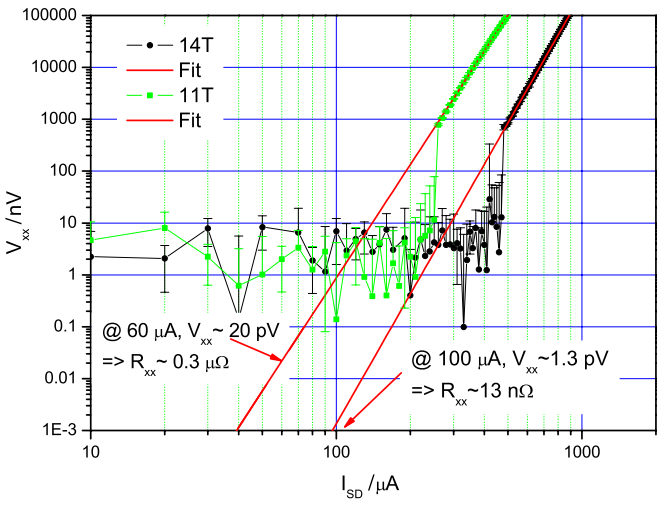

Figure 4. Log–log plot of V_{xx} as a function of source–drain current at 11 T (green squares) and 14 T (black dots). The red lines are fits to the data at high source–drain currents. 5 nV is the noise floor of the voltmeter.

magnetic flux density around 11 T. For these measurements a lower I_{sd} of 60 μA was chosen and a similar extrapolation of the high source–drain currents gives $V_{xx} \approx 20$ pV and $R_{xx} \approx 0.3\,\mu\Omega$.

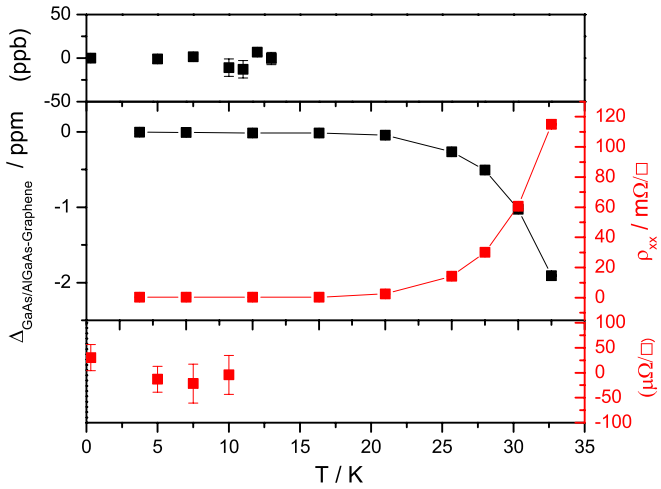

Figure 5. Middle: measurement of $\Delta_{\mathrm{GaAs/AlGaAs-graphene}} = [R_H(\mathrm{GaAs/AlGaAs}, T = 1.5\ \mathrm{K}) - R_H(\mathrm{graphene}, T)]/(R_K/2)$ and ρ_{xx} as a function of temperature for the graphene device. $B = 14$ T for the graphene device and 10.5 T for the GaAs/AlGaAs device. The measurement current was 60 μA. Top and bottom: high-resolution measurements of $\Delta_{\mathrm{GaAs/AlGaAs-graphene}}$ and ρ_{xx} demonstrating ppb-level quantization. For the middle panel the carrier density was 4.6×10^{11} cm^{-2} and for the top and bottom panels the density was 6.7×10^{11} cm^{-2}.

Returning to figure 3(b), we note that the measured I_c for contact pairs on either side of the device is virtually identical. I_c as a function of magnetic flux density shows a rather unusual dependence as the breakdown current continues to increase in the $\nu = 2$ quantum Hall state, reaching ≈500 μA at our maximum field of $B = 14$ T. This behaviour is very different from that observed in conventional semiconductor systems where the breakdown current peaks at the exact integer filling factor [4] indicated by the dashed blue line in figure 3(b). This behaviour can be explained by a magnetic field dependent charge transfer mechanism between the interfacial layer and graphene [30]. The amount of charge transfer is determined by the interplay of classical (as a result of the geometry) and quantum (as a result of the density of states) capacitance of the device structure. The density of states oscillates as the LLs pass through the Fermi level when the magnetic field increases. The result is that the carrier density in the graphene layer is also oscillating, and specifically when the Fermi level is between the $N = 0$ and $N = 1$ LLs, the carrier density increases linearly with magnetic field. This effectively pins the filling factor at $\nu = 2$ over a broad range of magnetic field, resulting in *a novel quantum Hall state which is ideally suited for high precision resistance metrology*. The anomalous pinning is responsible for the *extremely high breakdown current* and *wide operational parameter space* of an epitaxial graphene quantum Hall device.

Figure 5 demonstrates the robustness of the $\nu = 2$ quantum Hall state as a function of temperature. Here $\Delta_{\mathrm{GaAs/AlGaAs-graphene}} = [R_H(\mathrm{GaAs/AlGaAs}, T = 1.5\ \mathrm{K}) - R_H(\mathrm{graphene}, T)]/(R_K/2)$ quantifies the difference between the graphene sample and a fixed reference GaAs/AlGaAs device (the measurement technique is explained in detail in section 4). In a separate measurement the longitudinal resistivity was measured for the graphene device and plotted

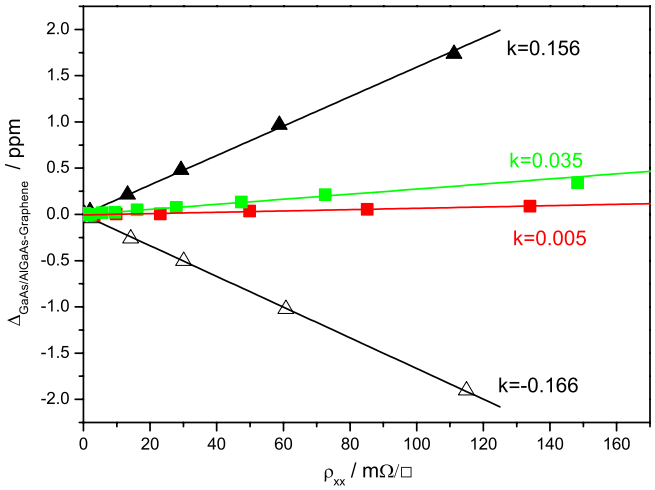

Figure 6. Variation of $\Delta_{\mathrm{GaAs/AlGaAs-graphene}}$ as a function of ρ_{xx} for three different charge carrier densities determined from data such as displayed in figure 5. Red $= 9.1 \times 10^{11}$ cm^{-2}, green $= 6.7 \times 10^{11}$ cm^{-2} and black $= 4.6 \times 10^{11}$ cm^{-2}. Open black triangles are measured in reverse field direction. Solid lines are fits to the data.

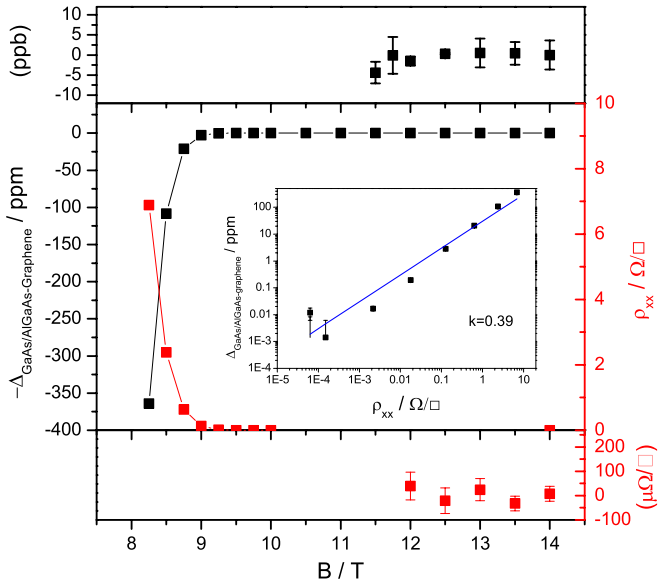

Figure 7. Middle: measurement of $-\Delta_{\mathrm{GaAs/AlGaAs-graphene}} = [R_{\mathrm{H}}(\mathrm{GaAs/AlGaAs}, B = 10.5\,\mathrm{T}) - R_{\mathrm{H}}(\mathrm{graphene}, B)]/(R_{\mathrm{K}}/2)$ and ρ_{xx} as a function of B on the graphene device. $T = 0.3$ K for the graphene device and 1.5 K for the GaAs/AlGaAs device. The measurement current was 60 μA. Top and bottom: high-resolution measurements of $-\Delta_{\mathrm{GaAs/AlGaAs-graphene}}$ and ρ_{xx} demonstrating ppb-level quantization. For the middle panel the carrier density was 4.6×10^{11} cm^{-2} and for the top and bottom panels the density was 6.7×10^{11} cm^{-2}. Inset: log–log plot of the variation of $\Delta_{\mathrm{GaAs/AlGaAs-graphene}}$ as a function of ρ_{xx} for the data in the middle panel.

in the same graph. The temperature for the reference device is held constant at 1.5 K while the temperature for the graphene device is varied. The middle panel of figure 5 shows a low resolution measurement across a wide temperature range and demonstrates that R_{H} starts to deviate as soon as a measurable ρ_{xx} appears. The top and bottom panels are high-resolution measurements which demonstrate ppb-level quantization up to 15 K when ρ_{xx} is of the order of several tens of μΩ (the high-resolution measurements were performed on an earlier cooldown cycle of the device when the charge carrier density was higher).

In figure 6 we have plotted $\Delta_{\mathrm{GaAs/AlGaAs-graphene}}$ versus ρ_{xx} for three separate cooldown cycles of the device. Each time $\Delta_{\mathrm{GaAs/AlGaAs-graphene}}$ is proportional to ρ_{xx}, identical to the well-known empirical relationship $\Delta R_H = k\rho_{xx}$ which has been observed for traditional semiconductor systems [4]. The value of k varies significantly between different runs which are signified by different charge carrier densities (in between cooldowns the sample was exposed to UV radiation in order to reduce the carrier density in small controllable steps). For the final and lowest charge carrier density we also measured k in the opposite magnetic field direction. The fact that the sign of k changes with the B-field direction indicates that the observed relation between R_{H} and ρ_{xx} is due to inhomogeneity of the charge density in the sample as proposed by van der Wel *et al* [29] rather than the finite width of the voltage probes for which no sign change is expected. In the latter case $k = \frac{l_p}{W} \approx 0.7$ for both B-field directions, which is clearly inconsistent with the experimental data. A plausible explanation for the increase in k with reducing carrier density could be the increase in inhomogeneity in the sample as we get closer to the Dirac point [1]. This is supported by the fact that the value of k was found to be different for different combinations of measurement contacts (not shown).

Combining the results from figure 4 where we estimated R_{xx} with the value of k obtained in figure 6 allows us to estimate the expected relative error in R_{H}. For $B = 14$ T and $I_{\mathrm{sd}} = 100$ μA we obtained $R_{xx} = 13$ nΩ, which with $k = 0.16$ implies that we can expect a relative error in R_{H} much less than 10^{-12}. Similarly for 60 μA at $B = 11$ T the relative error would be much less than 10^{-11}.

In figure 7 (middle) the same experiment as in figure 5 is repeated but this time with magnetic flux density as the parameter and $T = 300$ mK. The magnetic flux density for the reference device is held constant at the centre of the $\nu = 2$ plateau and the magnetic flux density for the graphene sample is varied. Top and bottom panels are high-resolution measurements which demonstrate ppb-level quantization (again measured on a different cooldown cycle). The graph shows that the $\nu = 2$ quantum Hall plateau extends over a range of at least 4 T and the measurement is only limited from above by the maximum available magnetic field. The inset is a log–log plot of $\Delta_{\mathrm{GaAs/AlGaAs-graphene}}$ as a function of ρ_{xx} similar to figure 6 and the blue line is $\Delta R_{\mathrm{H}} = k\rho_{xx}$ with $k = 0.39$. From the plot it can be seen that the data do not quite follow a linear dependence as might be expected. A likely reason for this deviation is the fact that as a function of B the charge carrier density in epitaxial graphene is not constant, which could result in a variation of k as a function of B.

Comparing the performance of our graphene device with that of GaAs devices shows a significantly wider operational parameter space for the $\nu = 2$ quantum Hall state. In GaAs the field range is usually a few tenths of a tesla up to 1 T for the best devices and for temperature the operational range is generally below 2 K [4, 38]. This result is not surprising

Table 2. Device parameters. The dimensions are defined in figure 1. The contacts on the PTB2 sample were made of small tin balls at the edges of the chip and so voltage probe width is not applicable.

Device	L/ mm	W/ mm	l/ mm	l_p/ mm	μ/ T^{-1}	n_s/ 10^{11} cm^{-2}
PTB2	6.0	2.5	~1.5	N/A	40	4.6
LEP	2.2	0.4	0.5	0.050	50	5.1
GR9	0.16	0.035	0.06	0.024	0.75	4.6

given the fact that the energy spacing between the $N = 0$ and $N = 1$ LLs is approximately seven times larger in graphene than in GaAs around a magnetic flux density of 10 T. Also the breakdown current in graphene compares favourably with that in GaAs. Although a breakdown current as large as 500 μA has been obtained in mesoscopic GaAs devices, our device is only 35 μm wide, at least a factor of ten narrower than standard Hall bars used for metrological measurements. This leaves significant scope for further improvement if wider, homogeneous, graphene devices can be produced. It is important to note that for the lowest charge carrier density ($\sim 4 \times 10^{-11}$ cm^{-2}) in our graphene device we have not yet reached the centre of the $\nu = 2$ quantum Hall plateau and the operational parameter space is likely to be even wider at higher magnetic flux densities or in devices with even lower charge carrier density.

3. Characterization of GaAs samples

The GaAs/AlGaAs heterostructures used in this work were standard Hall bar devices in use for routine quantum Hall metrology for the last 20 years at NPL and BIPM. One device was supplied originally by PTB (marked as PTB2) and the other by Laboratoires d'Électronique Philips (LEP). The dimensions and characteristic parameters are listed in table 2 together with those of the graphene device discussed in the previous section.

Before commencing the high-accuracy measurements both GaAs/AlGaAs samples were characterized according to the guidelines for quantum Hall resistance metrology [12] (i.e. we confirmed that the three-terminal contact resistance measured on the $\nu = 2$ plateau was of the order of a few ohms for all contacts used and that the longitudinal resistivity at the measurement current was below 10 μΩ). The breakdown current, I_c, measured at 1.5 K was 150 μA for the PTB2 device and 100 μA for the LEP device.

4. Cryogenic current comparator bridge

4.1. Design principle

The measurements were made with a cryogenic current comparator (CCC) bridge which has been described in detail in [19, 31] and is illustrated in a simplified form in figure 8. Isolated current sources 1 and 2 separately drive current through samples S_1 and S_2 and associated windings A and B on the CCC. The current ratio can be set via electronics to a few parts in 10^6 and this ratio is improved to a level of 1 part in 10^{11} by forming a negative feedback loop from the superconducting quantum interference device (SQUID) sensing the net flux in the CCC to one of the current sources. Our standard CCC uses the model A20 nanovolt amplifier manufactured by EM Electronics. The performance of this amplifier can be characterized as a voltage noise with Allan deviation of 0.14 nV and a current noise with Allan deviation of 0.2 pA for a 10 s observation (also see figure 4 in [31]). When measuring two quantum Hall devices with a combined impedance of ≈25 kΩ this current noise corresponds to 5 nV and dominates the resolution of the measurement system. We therefore chose to use a second CCC as a null detector [32]. The potential contacts on S_1 and S_2 are closed in a loop via winding C on this second CCC. This device is configured with just a single winding to measure a current null rather than two windings to establish a current ratio.

The CCC for the bridge current ratio is fitted with an RLC filter which is a modified version of the RC filter described in [19]. The modification gives a lower bandwidth of 1 kHz and was found to be necessary due to the larger interference experienced in this experiment involving four cryostats and long connecting cables between laboratories. Also, as a much higher accuracy was required for this precision comparison of quantum Hall samples than is needed for routine resistance measurement a guard, driven by a unity-gain operational amplifier, was added to the capacitors in the filter on each side of the bridge [33] to reduce any leakage across the CCC windings to a negligible level. The CCC for null detection was also fitted with a filter (at room temperature) to limit the bandwidth to approximately 16 kHz. The filter was constructed using 100 Ω resistors so as to keep the additional Johnson noise in the null detector circuit at the nanovolt level. The potential difference between the bridge circuit and the overall measurement system screen in the region of the null detector is held close to zero by the 100 kΩ resistor connected to the screen in the filter for current source 2. Any leakage resistance in the filter capacitors will therefore have a negligible effect and a guard circuit for these is not necessary.

The parameters for both CCCs are listed in table 3. The current sources and SQUID control units are connected to a computer which supervises the setting of the measurement currents and collects data from the two SQUIDs. Data are collected alternately in forward and reverse current directions so as to eliminate electrical offsets and drift.

4.2. Bridge sensitivity

The CCC bridge sensitivity can be derived from the schematic network in figure 8. At bridge balance the flux in the ratio CCC is zero so that $I_1 = I_2 = I$. A deviation of the ratio R_1/R_2 from unity will result in a small current, I_{ND}, in the null detector circuit. We have,

$$R_1(I - I_{ND}) = R_2(I + I_{ND}), \tag{1}$$

$$\frac{R_2}{R_1} = \frac{I - I_{ND}}{I + I_{ND}} \approx 1 - \frac{2I_{ND}}{I}. \tag{2}$$

The sensitivity of the null detector was checked by placing a 10 GΩ shunt resistor in parallel with one of the quantum Hall devices. For a measurement current of 100 μA a SQUID signal for the null detector CCC corresponding to $I_{ND} = 70$ pA was

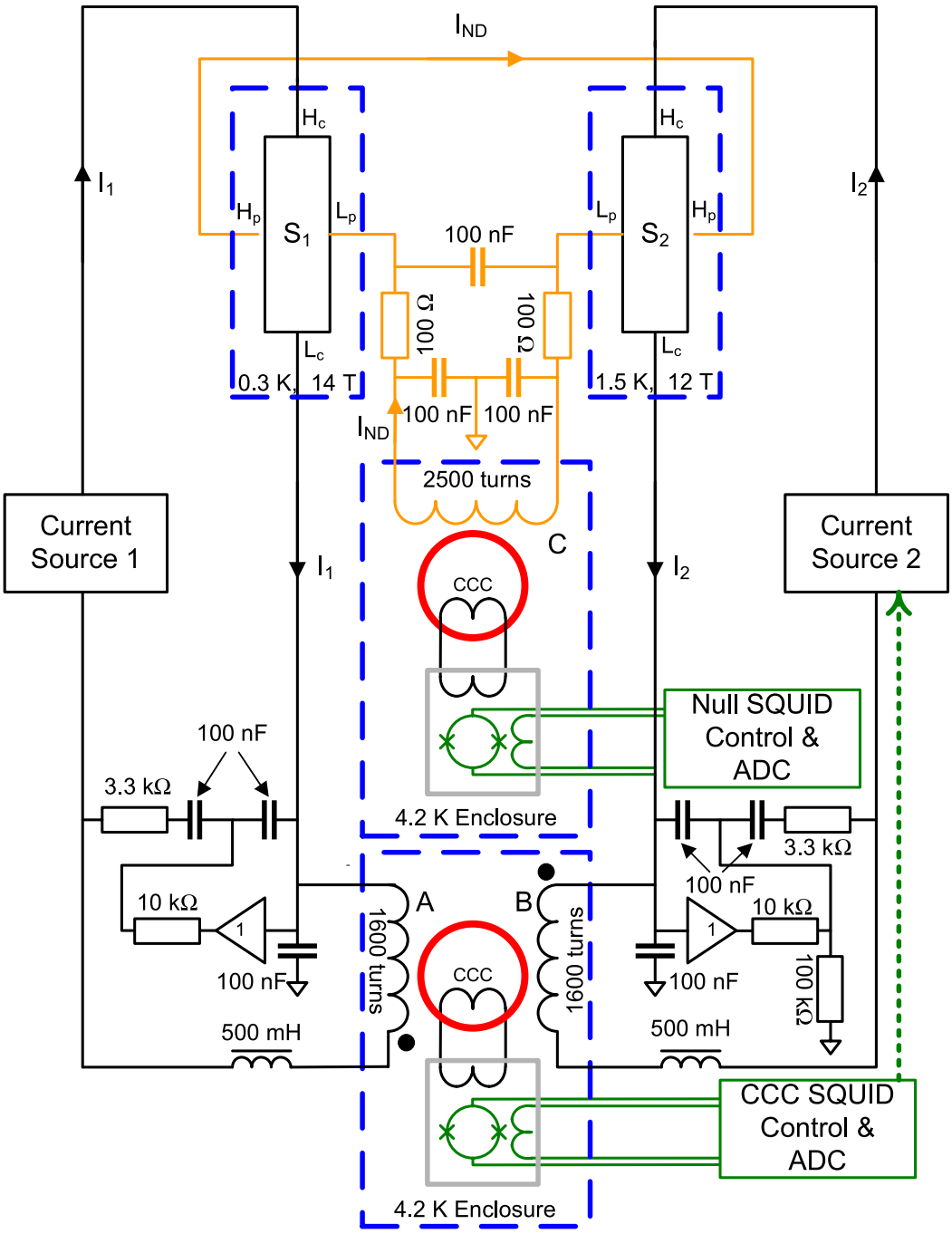

Figure 8. Schematic of the cryogenic current comparator bridge circuit.

observed which, according to equation (2), corresponds to a deviation of the resistance ratio from unity of 1.4×10^{-6}. This is in reasonable agreement with the calculated deviation of 1.3×10^{-6}, confirming the null detector sensitivity. A second feedback loop can be operated to bring the SQUID signal from the null detector to zero using a third winding on the CCC [19]. However, this is only necessary when an accurate resistance ratio measurement for resistors with deviations from nominal is required. In this experiment we are comparing two quantum Hall devices which are expected to be exactly equal to a very high degree, so this second feedback loop is not necessary and the open loop output of the null detector is simply recorded instead.

4.3. Noise and measurement resolution

The ultimate resolution of the bridge can be estimated by considering the noise components due to the current balance CCC, the null detector CCC and filter network, and the Johnson noise from the quantum Hall devices being measured. Here we use the Allan deviation of the time domain signals [19, 34] to analyse the various components. The design of the bridge is based on a noise performance of the dc SQUID and CCC combination with an Allan deviation of $10\,\mu\phi_0$ for a 10 s measurement interval. Table 3 lists the parameters for the different components of the bridge and the calculated voltage noise in the null detector loop in terms of the Allan deviation

Table 3. Summary of individual noise components in the bridge circuit and total expected noise. The noise attributed to the two CCCs is measured at 10 s and converted to voltage noise across one QHR device in the case of the current CCC and across two QHR devices for the voltage CCC. The noise arising from the resistors is calculated. The last two columns are the Allan deviation (AD) at a 10 s measurement time. Note that for white noise of power spectral density $h_0\,\mathrm{V^2\,Hz^{-1}}$ the corresponding Allan deviation is $(h_0/2\tau)^{-1/2}$.

Component	Comment	Sensitivity	CCC null AD/nV	A20 null AD/nV
Ratio CCC	1600 : 1600 t	16 μA turn ϕ_0^{-1}	1.3	1.3
Null CCC	2500 t	13 μA turn ϕ_0^{-1}	1.3	
A20 null	Voltage noise			0.14
A20 null	Current noise			5.0
QHR1	300 mK		0.1	0.1
QHR2	1.2 K		0.2	0.2
Filter	200 Ω		0.4	
Total			1.9	5.2

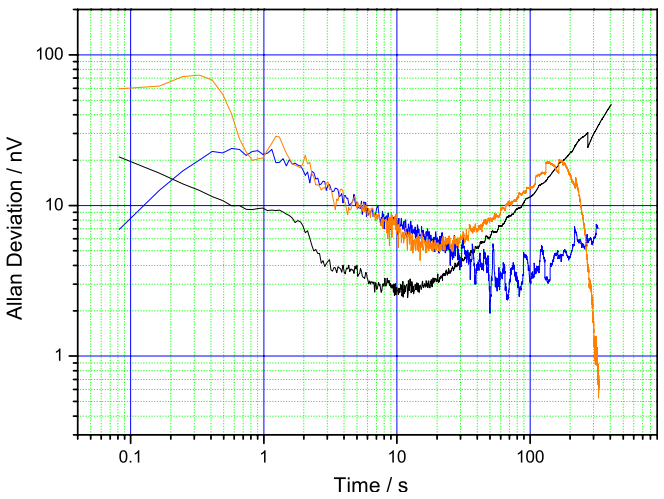

Figure 9. Allan deviation of the CCC nanovoltmeter (orange) and A20 nanovoltmeter (blue) when two QHR devices are connected to the bridge. Also shown is SQUID noise of the current balance CCC which was scaled to 1600 turns.

for a 10 s measurement interval. The total noise voltage for the bridge with the CCC nanovoltmeter is 1.9 nV compared with 5.2 nV when using the A20 nanovoltmeter.

Figure 9 shows the measured Allan deviation of the CCC null detector with two QHR devices connected to the bridge (the master and slave current sources and current balance CCC are disconnected). It is again expressed as a voltage noise in the null detector circuit. It can be seen from this graph that at 10 s the nanovoltmeter noise is approximately 8 nV compared with the design value of 1.3 nV. For comparison the measured Allan deviation is also shown for the A20 null detector which is similarly ∼8 nV at 10 s rather than the expected 5 nV. This suggests that both the CCC null detector and the A20 instrument are experiencing a similar level of excess noise. The enhancement of the noise is not surprising given the fact that we are using two quantum Hall systems each with their own magnet power supply and peripheral pumping equipment. In addition the connecting cables between these systems and

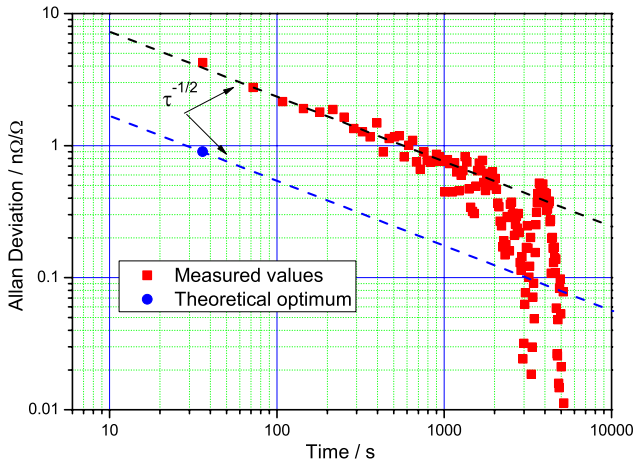

Figure 10. Typical Allan deviation of the resistance ratio for a 1 : 1 measurement of graphene against GaAs/AlGaAs heterostructure at $\nu = 2$ for a measurement current of 100 μA.

the measurement bridge span a distance of more than 10 m across two laboratories.

In figure 9 the noise from the current balance CCC is also shown and has been scaled for a 1600 turn winding and a single quantum Hall resistance to give an equivalent voltage noise in the null detector circuit. The Allan deviation goes through a minimum of ∼3 nV at about 10 s, which is again more than the expected 1.3 nV, and then increases at one decade per decade in the sampling interval. (Note that the minimum in the Allan deviation determines the optimum data acquisition time of ∼10 s in our measurement system.) Both SQUIDs exhibit a similar behaviour for time intervals longer than 30 s. The excess noise in the null detector circuit is clearly the limiting factor in our measurement system at present. Excess noise has also been seen in measurement systems of this type [32], and whereas in a manual data acquisition system the user can select apparently lower noise results, here our system runs for many hours unattended with the consequence that all data points are included in our analysis. From figure 9 we can conclude that the optimal measurement time is approximately 20 s for a given current direction. For longer times both the CCC null detector noise and current balance CCC noise contributions will start to increase, with the null detector at present dominating until time intervals longer than 50 s. A future improvement in this experiment would be to select a graphene and GaAs device with coinciding $\nu = 2$ plateaux which can be co-located in the same cryostat and thereby reduce the complexity of the connecting cables.

Figure 10 shows the Allan deviation for a 3.5 h measurement of graphene against GaAs at $\nu = 2$. The measurement data have been analysed in blocks of three intervals consisting of a 1 s settling time plus 10 s data collection interval (for optimum CCC performance) and a 1 s data transfer each to give a value for the resistance ratio every 36 s. (Note that the settling time for the CCC nanovoltmeter is much faster than that of the A20 where we have to allow for at least 10 s settling time [19]. We regularly checked the settling time by varying the wait-time after current reversal and inspecting the measurement result for systematic correlations.) Adding all the noise components in table 3 in quadrature

Table 4. Uncertainty budget.

Contribution	Uncertainty/ $p\Omega\,\Omega^{-1}$
Reproducibility	86
CCC ratio error	11
Leakage	10
Servo error	6
Miscellaneous	<1
Combined standard uncertainty	87

and using the observed noise for the CCC nanovoltmeter (which dominates) and current balance CCC in figure 9 gives a total noise of 8 nV for a 10 s measurement interval. For a measurement current of $\pm 100\,\mu A$ in $R_{K,\nu=2}$ this corresponds to a relative deviation of 3 parts in 10^9. This number can be related to a block of three intervals by multiplying by a scaling factor of $\sqrt{3/2}$ [19] to give 4 parts in 10^9 for the expected Allan deviation. From figure 10 we see that the first data point is also at 4 parts in 10^9, confirming that the overall measurement resolution is consistent with the measured noise. The Allan deviation decreases as $1/\sqrt{\tau}$ as expected for white noise and shows that the current reversal technique efficiently removes the non-white noise visible in figure 9. After 3.5 h measurement time a relative uncertainty of 2 parts in 10^{10} is achieved. If the two CCCs can be made to operate at their optimum noise performance, a single block of three measurements would give a relative uncertainty slightly better than 1 part in 10^9 and 6 parts in 10^{11} after 3.5 h (blue dot and dashed line in figure 10).

5. Uncertainty analysis

5.1. Type B analysis

5.1.1. Ratio error. The ratio error is determined by connecting both 1600 turn windings in series opposition. A large (10 mA) current is passed through the windings and the SQUID signal recorded (total applied current linkage is 32 A turn). This process is repeated several hundred times in both forward and reverse current directions to improve the measurement resolution. A least-squares fit to the data gives $(17 \pm 7)\,\mu V$ for the residual SQUID signal. The sensitivities of the SQUID and CCC are $0.7\,V\phi_0^{-1}$ and $16\,\mu A\,\text{turn}\,\phi_0^{-1}$, respectively, giving an imbalance of $(3.6 \pm 0.9) \times 10^{-10}$ A turn. In principle it is possible to correct the measurement results for this imbalance because it is a fixed property of the CCC. However, given the small size we have not done this and have used the imbalance as an uncertainty component, resulting in a relative standard uncertainty of 1.1×10^{-11} in the uncertainty budget (table 4).

5.1.2. Leakage. Leakage resistances must be controlled to a very high level in precision resistance measurements depending on where they appear in the bridge circuit. The most stringent condition occurs for the wiring connecting the device in the cryogenic system to the bridge. A leakage between the high and low potential sides of the device would appear as a resistance in parallel with the quantum Hall device and result in a direct error. Given that the quantum Hall resistance at $\nu = 2$ is approximately $10^4\,\Omega$, this implies a leakage $\geqslant 10^{15}\,\Omega$ for a relative error less than 10^{-11}. Measuring such a large resistance on long leads (there is no screen between high and low potential leads for ~3 m from the top of the cryostat probe to the sample in the 14 T/300 mK system at NPL) is not straightforward. Using a Keithley 6430 electrometer and a repeated ± 100 V excitation during a 10 h measurement resulted in (0.1 ± 0.06) pA, giving a relative standard uncertainty of 1×10^{-11} in the uncertainty budget.

5.1.3. Servo error. Any residual error in the current ratio between master and slave will translate directly into a false reading on the null detector. In order to test and correct for this error, we record the residual SQUID voltage from the current balance CCC during measurements. From this we can calculate the resulting current in the null detector CCC via

$$I_{SQ}^{ND} = \alpha V_{SQ}$$
$$\alpha = \frac{16\,\mu A\,\text{turn}\,\phi_0^{-1}}{2 \times 1600 \times 0.7\,V\phi_0^{-1}} \approx 7 \times 10^{-9}\,A\,V^{-1}. \quad (3)$$

and apply a correction. Typically we find corrections in the range $\sim(3 \pm 0.6)$ fA, which corresponds to a relative correction of (3 ± 0.6) parts in 10^{11} to the resistance ratio for a measurement current of 100 μA. The reason this small error arises is that the slave current source drifts very slightly relative to the master source after each current reversal, due to self-heating in the current source components. The feedback servo has a single integral term so a linear drift in the current source translates into a steady error voltage at the output of the SQUID. For our system, the residual error current in the CCC of ~3 fA quoted above corresponds to an open loop drift in the current sources of approximately 1 part in 10^6 over the period of a 20 s measurement.

5.1.4. Miscellaneous. In the comparison measurements are performed in sets of ten intervals of successive forward and reverse currents (rather than the shorter blocks of three intervals which were used in the previous section to analyse the time evolution of the Allan deviation). Each data set is written to disk and a new measurement started. Typically this operates for many hours and hundreds of data sets are collected. Each data set of ten intervals is analysed using a least-squares fitting routine to give a value for the resistance ratio and standard deviation. The residuals of the fit are analysed in order to observe potential problems with the system such as excessive settling time, noise and interference.

Figure 11(*a*) shows the average of 300 sets of fit residuals (i.e. 10 h total measurement time) and a marked oscillation becomes visible in the data (indicated by the green curve). The oscillation starts at the first forward current measurement interval and damps out with a time constant of about 60 s. We speculate that this effect is caused by a slight heating of the CCC helium dewar due to the measurement current. Normally we start a measurement set from zero current and ramp to maximum forward current, collect data, ramp to maximum

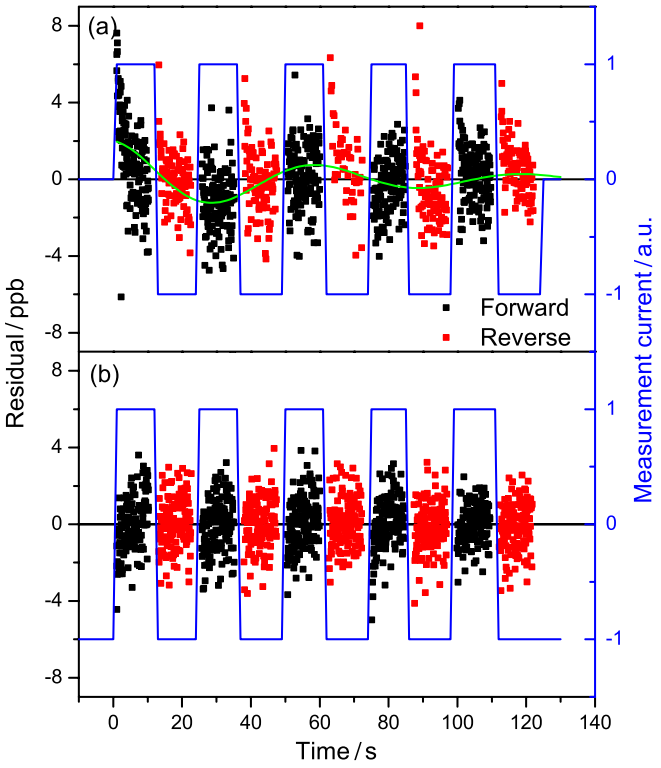

Figure 11. (*a*) Average of fitting residuals for 300 measurement sets using our standard measurement sequence (blue curve) and (*b*) modified sequence. Green curve in (*a*) is a guide to the eye.

reverse current, etc (blue curve in figure 11(*a*)). A current reversal takes approximately 1 s. At the end of a measurement set the current is ramped back to zero, data written to file and a new measurement started, which combined takes about 6 s, i.e. the current is zero for 6 s between measurement sets. Because the down-leads to the CCC are not superconducting, dissipation occurs during the measurement, and drops for 6 s between measurement sets, causing a temperature–pressure oscillation in the dewar. Averaging the residuals in figure 11(*a*) results in an error of $\sim 1 \times 10^{-10}$, which is not insignificant for our comparison.

Figure 11(*b*) displays the average of a similar 10 h measurement where the measurement current was always present in the CCC (i.e. the measurement current was left at maximum reverse current at the end of a measurement set and the new set would start by sweeping from reverse to forward maximum current). As can be seen from this graph the oscillation has disappeared and the mean of all residuals averages to 3×10^{-15} and any remaining error is therefore negligible.

This effect demonstrates the care that must be taken when making very high precision measurements and the power of automated measurements and data analysis in tracking down extremely small systematic errors.

6. Type A analysis

The automated measurement system allows us to make continuous measurements over many hours (usually during the night) so that the statistics on the final answer can be improved. Figure 12 shows a histogram of all CCC null detector values, expressed in terms of the voltage at the SQUID output, obtained from individual data sets of ten current reversals. The SQUID output voltage is the correct parameter to combine to give a distribution, since the noise recorded by this detector does not depend on the measurement current in the bridge (the data consist of sets at several different measurement current values). The total number of data sets for the complete measurement campaign was 2300, equating to almost 100 h of data collection. The solid line is a least-squares Gaussian fit to the histogram and gives a value of 245 µV for the standard deviation. Using the SQUID amplifier gain and the sensitivity values in table 3, the standard deviation of 245 µV translates to a current I_{ND} of 150 fA. Finally, using equation (2) and a measurement current of 100 µA, this standard deviation is equivalent to a relative deviation of 3.1×10^{-9} in the resistance ratio. Since the measurements were done at a range of currents, an effective number of measurements has to be calculated from

$$N_{\mathrm{eff}} = \sum n_i I_0^2 / I_i^2 \tag{4}$$

where $I_0 = 100\,\mu\mathrm{A}$, and n_i is the number of measurements taken at measurement current I_i. This equation gives $n_{\mathrm{eff}} = 1057$ in our case, and dividing the relative uncertainty by the square root of this number leads to a final type A uncertainty for the entire data set of 9.4×10^{-11} compared with 8.6×10^{-11} obtained in the next section.

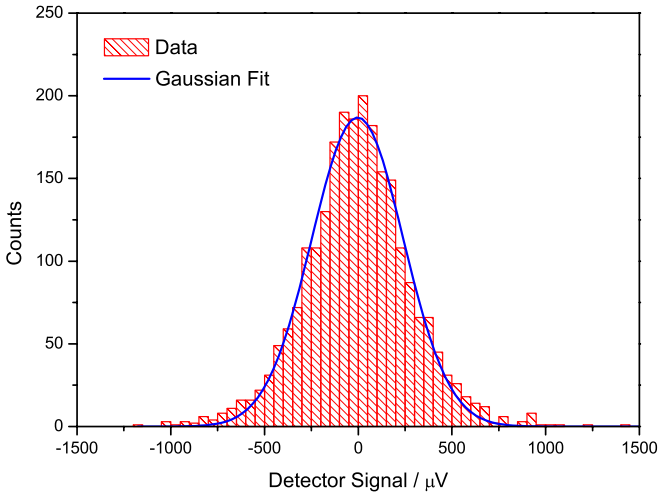

Figure 12. Histogram of null detector signal and Gaussian fit.

7. Comparison result

In order to test the universality of the QHE, two different devices need to be set up at the same quantum Hall plateau so that a one-to-one comparison of resistance can be made (in principle one could also compare different index plateaux if different ratios are available on the CCC). Unfortunately, the quantum Hall plateaux of the graphene and the GaAs/AlGaAs devices do not overlap and two cryostats have to be used for this experiment, one of which was the travelling quantum Hall system of the BIPM. Hartland *et al* [35] used a clever method

of tilting one device with respect to the magnetic field direction to make the centres of the plateaux in GaAs and Si occur at the same magnetic field, a trick not currently possible in our quantum Hall probe. As explained in the previous section using two cryostats does lead to a significant increase in noise and subsequent lengthening of the measurement time.

The graphene sample was mounted in a 14 T/300 mK cryostat and connected to the slave side of the CCC bridge. Two GaAs/AlGaAs samples were mounted in the transportable 11.7 T/1.5 K cryostat provided by the BIPM and connected to the master side. Prior to making comparison measurements all samples were fully characterized [12]. For the graphene sample the $B_{\nu=2}$ was set to 14 T, our maximum available magnetic field, and either 9.5 T or 10.5 T for samples PTB2 and LEP, respectively. The winding ratio on the bridge was always 1600 : 1600 turns. The red triangles in figure 13 are the results for GR9 against PTB2 for four different source–drain currents in the devices (using contacts 2 and 7 on the graphene device for R_{H} and contacts 4 and 5 on the GaAs device[6]). The pink diamond is a measurement for GR9 against LEP at $I_{\mathrm{sd}} = 50\,\mu\mathrm{A}$ (using the same contact configuration as for the red triangle measurements). Here $\Delta_{\mathrm{GaAs/AlGaAs-graphene}} = [R_{\mathrm{H}}(\mathrm{GaAs/AlGaAs}) - R_{\mathrm{H}}(\mathrm{graphene})]/(R_{\mathrm{K}}/2)$ and each data point consists of an average of between 3 h and 10 h worth of data. The uncertainty increases for lower I_{sd} because the signal-to-noise ratio is worse for lower I_{sd}.

To eliminate the possibility of errors due to non-zero ρ_{xx} we repeated a number of these measurements for non-opposite contacts. Note that it is very difficult to measure ρ_{xx} directly to the required level of precision (see, for example, figure 4). The green dot is a measurement using contacts 3 and 4 for R_{H}(GaAs/AlGaAs) on the PTB2 device at $I_{\mathrm{sd}} = 100\,\mu\mathrm{A}$. The blue square is a measurement using contacts 2 and 4 for R_{H}(graphene) on the graphene device at $I_{\mathrm{sd}} = 75\,\mu\mathrm{A}$. Another test to check for small errors is to reverse the direction of magnetic field on the graphene sample. The result of this measurement is represented by the light blue hexagon for $I_{\mathrm{sd}} = 60\,\mu\mathrm{A}$ (using the same contact configuration as for the red triangle measurements). Finally, the devices were exchanged between the NPL and BIPM cryostats in order to check for small parasitic leakages (the magnetic field was set to 11.5 T for the graphene device in the BIPM cryostat). This data point is shown as the black square in figure 13 (using the same contact configuration as for the red triangle measurements).

The data in figure 13 show no sign of any systematic errors in the measurement campaign and so all results can be combined to give a weighted mean of $\Delta_{\mathrm{GaAs/AlGaAs-graphene}} = (-4.7 \pm 8.6) \times 10^{-11}$. Combining this with the total type B uncertainty determined in section 5.1 gives 8.7×10^{-11} as a final combined uncertainty on the difference between R_{H}(GaAs/AlGaAs) and R_{H}(graphene)[7].

[6] The contact labels for the GaAs devices are the same as for the graphene device depicted in figure 1.

[7] This relative uncertainty is fractionally larger (0.1×10^{-11}) than the one published in [20] due to a more thorough determination of the systematic components.

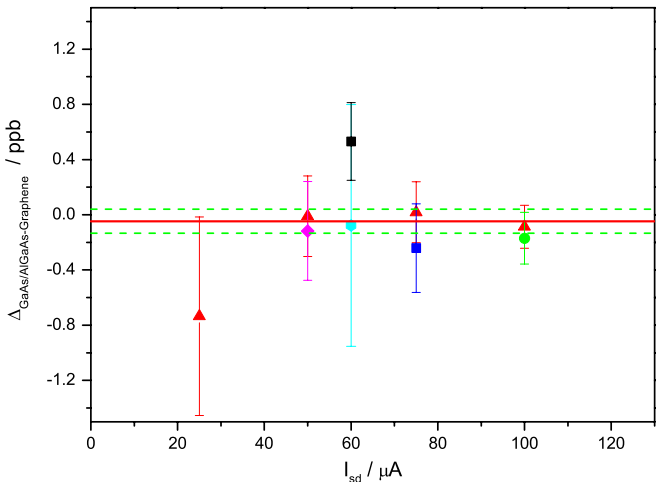

Figure 13. Measurement of $\Delta_{\mathrm{GaAs/AlGaAs-graphene}}$ for the direct comparison of R_{H}(GaAs/AlGaAs) and R_{H}(graphene) as a function of I_{SD}. The uncertainty bars represent the $\pm 1\sigma$ standard deviation of the mean. Different symbols are explained in the text. The red line is the weighted mean of all the data points and the green lines signify $\pm 1\sigma$.

8. Conclusion

Previously our knowledge of the universality of the QHE has been limited to the level of $(2\text{–}3) \times 10^{-10}$ for comparisons between GaAs and Si or between identical GaAs devices [35–38]. However both GaAs and Si are traditional semiconductors with a parabolic bandstructure and governed by the same physics. Graphene is a semi-metal with a linear bandstructure and is described by Dirac-type massless charge carriers and so universality in terms of material independence goes well beyond the comparison between two semiconductors. It does directly support the Thouless–Laughlin argument [7] that the Hall conductivity is a topological invariant and is a fundamental test of condensed matter theory.

Our results on material independence are the strongest evidence yet that the hypothesis that the resistance is quantized in units of h/e^2 is correct and thereby supports the pending redefinition of the SI units kilogram and ampere in terms of h and e. Note that the correctness of this equation can only be shown in a comparison of R_{H} with an independent realization of h/e^2, for example via the Thompson–Lampard capacitance [39]. However, the relative uncertainty which can be obtained in such an experiment is some 3 orders of magnitude worse than in a test of the material independence.

In our universality experiment the maximum source–drain current that the GaAs device can sustain without dissipation limits the measurement uncertainty, whereas a potentially lower uncertainty can be obtained in a consistency check of two graphene devices. Also the measurement system could still be significantly improved by reducing the excess noise or by adopting a different measurement technique such as demonstrated in [37].

The journey from the original discovery of the QHE in graphene to a quantum resistance standard which outperforms the established technology in many aspects has been remarkably short. For epitaxial graphene the robustness of

the quantization in terms of temperature, magnetic field and source–drain current is exceptional. The material is cheap and relatively easy to fabricate and process. It allows for the realization of a quantum resistance standard with modest means, e.g. a small superconducting magnet and cryocooler. As such it will improve the proliferation of quantum standards and allow many smaller laboratories to realize their own resistance scale. One even could envisage university students being able to perform QHE experiments, much in the same way as the discovery of high-T_c superconductors enabled table-top experiments with Josephson junctions in many science classes.

Acknowledgments

The authors are grateful to Dale Henderson, Stephen Giblin and Pravin Patel for their valuable contributions during this work. This work was supported by the UK NMS Pathfinder Programme, Swedish Research Council and Foundation for Strategic Research, EU FP7 STREPs ConceptGraphene and SINGLE, EPSRC grant EP/G041954 and the Science and Innovation Award EP/G014787.

References

[1] Novoselov K S, Geim A K, Morozov S V, Jiang D, Katsnelson M I, Grigorieva I V, Dubonos S V and Firsov A A 2005 Two-dimensional gas of massless Dirac fermions in graphene *Nature* **438** 197–200

[2] Zhang Y B, Tan Y W, Stormer H L and Kim P 2005 Experimental observation of the quantum Hall effect and Berry's phase in graphene *Nature* **438** 201–4

[3] For a review, see Prange R E and Girvin S M 1990 *The Quantum Hall Effect* (Berlin: Springer)

[4] Jeckelmann B and Jeanneret B 2001 The quantum Hall effect as an electrical resistance standard *Rep. Prog. Phys.* **64** 1603–55

[5] Geim A K 2009 Graphene: status and prospects *Science* **324** 1530–4

[6] Novoselov K S, Jiang Z, Zhang Y, Morozov S V, Stormer H L, Zeitler U, Maan J C, Boebinger G S, Kim P and Geim A K 2007 Room-temperature quantum Hall effect in graphene *Science* **315** 1379–9

[7] Thouless D J 1994 Topological interpretations of quantum Hall conductance *J. Math. Phys.* **35** 5362–72

[8] Hehl F W, Obukhov Y N and Rosenow B 2004 Is the quantum Hall effect influenced by the gravitational field? *Phys. Rev. Lett.* **93** 096804

[9] Penin A A 2009 Quantum Hall effect in quantum electrodynamics *Phys. Rev.* B **79** 113303

[10] Mohr P J, Taylor B N and Newell D B 2008 CODATA recommended values of the fundamental physical constants: 2006 *Rev. Mod. Phys.* **80** 633–730

[11] Mills I M, Mohr P J, Quinn T J, Taylor B N and Williams E R 2011 Adapting the international system of units to the twenty-first century *Phil. Trans. R. Soc. Math. Phys. Eng. Sci.* **369** 3907–24

[12] Delahaye F and Jeckelmann B 2003 Revised technical guidelines for reliable dc measurements of the quantized Hall resistance *Metrologia* **40** 217–23

[13] Giesbers A J M, Rietveld G, Houtzager E, Zeitler U, Yang R, Novoselov K S, Geim A K and Maan J C 2008 Quantum resistance metrology in graphene *Appl. Phys. Lett.* **93** 222109

[14] Shen T, Gu J J, Xu M, Wu Y Q, Bolen M L, Capano M A, Engel L W and Ye P D 2009 Observation of quantum-Hall effect in gated epitaxial graphene grown on SiC (0 0 0 1) *Appl. Phys. Lett.* **95** 172105

[15] Wu X S, Hu Y K, Ruan M, Madiomanana N K, Hankinson J, Sprinkle M, Berger C and de Heer W A 2009 Half integer quantum Hall effect in high mobility single layer epitaxial graphene *Appl. Phys. Lett.* **95** 223108

[16] Tzalenchuk A, Lara-Avila S, Kalaboukhov A, Paolillo S, Syvajarvi M, Yakimova R, Kazakova O, Janssen T J B M, Fal'ko V and Kubatkin S 2010 Towards a quantum resistance standard based on epitaxial graphene *Nature Nanotechnol.* **5** 186–9

[17] Jobst J, Waldmann D, Speck F, Hirner R, Maude D K, Seyller T and Weber H B 2010 Quantum oscillations and quantum Hall effect in epitaxial graphene *Phys. Rev.* B **81** 195434

[18] Tanabe S, Sekine Y, Kageshima H, Nagase M and Hibino H 2010 Half-integer quantum Hall effect in gate-controlled epitaxial graphene devices *Appl. Phys. Express* **3** 075102

[19] Williams J M, Janssen T J B M, Rietveld G and Houtzager E 2010 An automated cryogenic current comparator resistance ratio bridge for routine resistance measurements *Metrologia* **47** 167–74

[20] Janssen T J B M, Fletcher N E, Goebel R, Williams J M, Tzalenchuk A, Yakimova R, Lara-Avila S, Kubatkin S and Fal'ko V I 2011 Graphene, universality of the quantum Hall effect and redefinition of the SI system *New J. Phys.* **13** 093026

[21] Woszczyna M, Friedemann M, Pierz K, Weimann T and Ahlers F J 2011 Magneto-transport properties of exfoliated graphene on GaAs *J. Appl. Phys.* **110** 043712

[22] Guignard J, Schopfer F, Poirier W and Glattli D C 2011 Quantum Hall effect in exfoliated graphene on Si/SiO_2 from metrological measurements arXiv:1110.4884v1

[23] Virojanadara C, Virojanadara C, Syvajarvi M, Yakimova R, Johansson L I, Zakharov A A and Balasubramanian T 2008 Homogeneous large-area graphene layer growth on 6H-SiC(0 0 0 1) *Phys. Rev.* B **78** 245403

[24] Kopylov S, Tzalenchuk A, Kubatkin S and Fal'ko V I 2010 Charge transfer between epitaxial graphene and silicon carbide *Appl. Phys. Lett.* **97** 112109

[25] Lara-Avila S, Moth-Poulsen K, Yakimova R, Bjornholm T, Fal'ko V, Tzalenchuk A and Kubatkin S 2011 Non-volatile photochemical gating of an epitaxial graphene/polymer heterostructure *Adv. Mater.* **23** 878–82

[26] Lara-Avila S, Tzalenchuk A, Kubatkin S, Yakimova R, Janssen T J B M, Cedergren K, Bergsten T and Fal'ko V 2011 Disordered Fermi liquid in epitaxial graphene from quantum transport measurements *Phys. Rev. Lett.* **107** 166602

[27] Yoshioka D 2002 *The Quantum Hall Effect* (Berlin: Springer)

[28] Cage M E, Dziuba R F, Field B F, Williams E R, Girvin S M, Gossard A C, Tsui D C and Wagner R J 1983 Dissipation and dynamic nonlinear behavior in the quantum Hall regime *Phys. Rev. Lett.* **51** 1374

[29] van der Wel W, Harmans C J P M and Mooij J E 1988 A geometric explanation of the temperature dependence of the quantised Hall effect *J. Phys. C: Solid State Phys.* **21** L171–5

[30] Janssen T J B M, Tzalenchuk A, Yakimova R, Kubatkin S, Lara-Avila S, Kopylov S and Fal'ko V I 2011 Anomalously strong pinning of the filling factor $\nu = 2$ in epitaxial graphene *Phys. Rev.* B **83** 233402

[31] Williams J M, Rietveld G, Houtzager E and Janssen T J B M 2011 Design considerations for a CCC bridge with complete digital control *IEEE Trans. Instrum. Meas.* **60** 3907–12

[32] Delahaye F and Bournaud D 1991 Low-noise measurements of the quantized Hall resistance using an improved cryogenic

current comparator bridge *IEEE Trans. Instrum. Meas.* **40** 237–40
[33] Williams J M and Hartland A 1991 An automated cryogenic current comparator resistance ratio bridge *IEEE Trans. Instrum. Meas.* **40** 267–70
[34] Witt T J and Reymann D 2000 Using power spectra and Allan variances to characterise the noise of Zener-diode voltage standards *IEE Proc. Sci. Meas. Technol.* **147** 177–82
[35] Hartland A, Jones K, Williams J M, Gallagher B L and Galloway T 1991 Direct comparison of the quantized Hall resistance in gallium-arsenide and silicon *Phys. Rev. Lett.* **66** 969–73
[36] Jeckelmann B and Jeanneret B 1997 High-precision measurements of the quantized Hall resistance: experimental conditions for universality *Phys. Rev.* B **55** 13124–34
[37] Schopfer F and Poirier W 2007 Testing universality of the quantum Hall effect by means of the Wheatstone bridge *J. Appl. Phys.* **102** 054903
[38] Poirier W and Schopfer F 2009 Resistance metrology based on the quantum Hall effect *Eur. Phys. J.—Special Topics* **172** 207–45
[39] Bachmair H 2009 Determination of the unit of resistance and the von Klitzing constant R_K based on a calculable capacitor *Eur. Phys. J.—Special Topics* **172** 257–66